Results in Engineering 24 (2024) 103566

Contents lists available at ScienceDirect

Results in Engineering

journal homepage: www.sciencedirect.com/journal/results-in-engineering

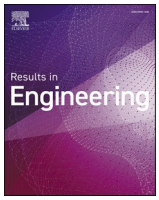

Research paper

Experimental and numerical analyses of the hemodynamics impact on real intracranial aneurysms: A particle tracking approach

A. Souza [a,b,e], D. Lopes [b], S. Souza [a], J. Ribeiro [e,f], R.A. Lima [a,c,g], C. Ferrera [d,*]

[a] MEtRICs, Mechanical Eng. Dep., Univ. of Minho, Campus de Azurém, Guimarães, Portugal
[b] CMEMS-UMinho, Mechanical Eng. Dep., Univ. of Minho, Campus de Azurém, Guimarães, Portugal
[c] CEFT, Faculdade de Eng. da Univ. do Porto (FEUP), Porto, Portugal
[d] Depto. de Ingeniería Mecánica, Energética y de los Materiales and ICCAEx, Univ. Extremadura, Spain
[e] Centro de Investigação de Montanha (CIMO), Instituto Politécnico de Bragança, Campus de Santa Apolónia, Bragança, Portugal
[f] Laboratório Associado para a Sustentabilidade e Tecnologia em Regiões de Montanha (SusTEC), Instituto Politécnico de Bragança, Campus de Santa Apolónia, Bragança, Portugal
[g] Associate Laboratory in Chemical Engineering (ALiCE), Faculty of Engineering, University of Porto, 4200-465 Porto, Portugal

ARTICLE INFO

Keywords:
Intracranial aneurysms
Particle tracking velocimety (PTV)
Computational Fluid Dynamics (CFD)
Hemodynamics
Blood flow
PDMS biomodel

ABSTRACT

This study investigates the impact of hemodynamics on real intracranial aneurysms (IAs) using experiments and computational fluid dynamics (CFD) simulations. A particle tracking velocimetry (PTV) approach was used to study the vortical structures inside a real aneurysm and validate numerical simulations performed at a steady regime for different flow rates. Moreover, this and two additional patient-specific cases have been numerically analyzed, focusing on flow patterns, wall shear stress (WSS), relative residence time (RRT), and oscillatory shear index (OSI) for transient studies. For the transient simulations, vorticity profiles indicated significant rotation of fluid particles in the neck and outlet arteries. TAWSS analysis revealed high WSS values in the bifurcation zone, neck, and middle cerebral artery (MCA), with variations among the patients. OSI and RRT plots provided insights into disturbed flow patterns, low or oscillatory WSS areas, and regions with prolonged residence time. This study shows great potential for combining PTV and CFD to obtain detailed insights into flow structures in aneurysms, which are crucial to developing effective treatments and interventions for IA management.

1. Introduction

Disorders in the cardiovascular system are one of the major causes of death worldwide. Ischemic heart and cerebrovascular diseases originate >85 % of the deaths in this system [1]. Cerebrovascular disorders rank second globally and first in Southeast and East Asia [1].

Intracranial aneurysms (IA) are one of the causes of fatalities from cerebrovascular disease. Local intracranial artery dilations are known as IAs [2]. IAs can be found in as much as 3.2 % of people [3]. Of these IAs, 0.25 percent will break and bleed through the subarachnoid space [4]. The death rate from hemorrhaging can exceed 60 %, and <40 % of survivors are dependent [5]. Flow through IAs can be excluded [6] or diverted [7] by applying different technologies. These treatments come with significant hazards and financial costs for the health system that will rise due to population aging [8].

Therefore, it is crucial to comprehend the processes that start IAs development and the breach of the vessel wall. According to scientists, many circumstances, including hereditary conditions, mycotic infections, hypertension, breathing cigarette smoke, drinking alcohol, and simply becoming older, can cause an IA to manifest and develop [9,10]. The characteristics and flow behavior of the original artery wall are modified due to these changes. A vicious loop involving the wall deterioration and its subsequent restoration, as well as other alterations in the flow, is caused by the sensitivity of the cells of the endothelium to the flow changes [11], which initiates various biological processes [12,13,14]. A new geometry will develop based on the level of degradation of the wall, the point of maximum weakness, the blood stresses, the adjacent walls, and potential inflammatory mechanisms. This geometry can be stable or grow as an aneurysm that may have a breach [15].

These complex processes must still be understood. A small group

* Corresponding author.
E-mail address: cfll@unex.es (C. Ferrera).

https://doi.org/10.1016/j.rineng.2024.103566
Received 12 May 2024; Received in revised form 8 October 2024; Accepted 26 November 2024
Available online 28 November 2024

considers that geometry is most important when an IA risk and its treatment are evaluated in clinical practice [16]. However, most scientific community agrees that hemodynamics plays the most prominent role [15,17].

Three approaches are being employed to understand these processes: in vivo, in vitro, and *in silico* studies.

Transcranial Doppler (TCD) ultrasounds, magnetic resonance angiographies (MRA), and 4D computed tomography angiographies (4D-CTA) are the most employed non-invasive techniques to measure the flow in alive organisms. TCD is a solid approach but provides indirect measurements and is not eligible for any artery or subject [18,19]. Moreover, TCD signals present noise that must be processed to get the underlying flow features [20]. 4D-CTA is evolving [21], and MR routines are the most popular. MRA can measure vessels' laminar Wall Shear Stress (WSS) [22]. WSS calculates the force the blood exerts on the vessel endothelium. This parameter is crucial to understand IA hemodynamics. It can be obtained through MR and compared with numerical simulations [23]. However, MR-based measurements undervalue WSS [23–25] and cannot provide a good definition in small-size arteries [24] or wall-adjacent areas [26].

While in vivo procedures are improving, both *in silico* and in vitro approaches have significantly improved. Computational Fluid Dynamics (CFD) in IAs can give doctors helpful information from non-invasive measures. Early studies have computed the WSS in regions where aneurysm formation is more likely to occur (e.g., bifurcations or highly curved arteries) [27]. This ground-breaking research using radiograph-extracted geometries in 2D steady simulations [28] has rapidly developed. For example, numerical simulations have been conducted under more realistic circumstances: 3D actual geometries [29] non-steady flow [30], real patient flow conditions [31], and flexible walls [32,33] have all been gradually adopted. Also, numerical studies have been conducted to understand the flow in geometries with multiple aneurysms [34], the influence of a wall with protrusions in the surface [35], the regions where thrombi can appear [36] or new endovascular techniques such as flow diversion or coiling [37–39].

From a numerical point of view, it is also essential to assess the prediction capability of scientific groups. A contest was held to analyze the accuracy of several methodologies when analyzing identical geometries [40]. The main conclusion achieved is that numerical results must be experimentally validated as predictions are not uniform [40,41].

Manufactured aneurysm models can be employed for experimental validation. Glass-manufactured aneurysms [42] or silicone ones [43] were initially introduced. Then, more evolved rigid low-cost polydimethylsiloxane (PDMS) real models were manufactured [44]. Models can be employed for analysis [45] or training in endovascular techniques [46]. Flexible models are available in ideal IA geometries [47,48].

Regarding the techniques for in vitro flow analysis, MR, Laser Doppler Anemometry (LDA), and Particle Image Velocimetry (PIV) are employed. MR and LDA studies are scarce. As stated previously, low resolution hinders the applicability of MR for flow measurements [24,26], even though filters have been introduced to incorporate them into numerical simulations [49]. PIV is the most common experimental choice for the moment.

PIV measurements in idealized geometries showed that the IA morphology influences the aneurysm flow distribution [16]. This distribution also changes with the wall properties [48] and the orientation of the inlet parent arteries [50]. Those idealized geometries must be manufactured carefully to be compared against numerical simulations, as slight differences are transferred to comparing the results [16].

Experiments in models manufactured from segmented patient geometries have the added difficulty of matching the segmented geometry with the final model. Rolloff et al. 2018 [24] have compared several experimental techniques (MRI, PIV, stereo PIV, tomo PIV) and CFD. They have reported that velocity MRI results lack enough resolution but can be cautiously considered. Although MR velocity measurement accuracy can be estimated [51], WSS measurements are seriously affected due to that limitation [25], and methods are being proposed to improve this accuracy [52]. Tomo PIV 3D velocity measurements constitute a remarkable visualization tool. Nevertheless, require high computational time, and both vector gradients and fine structures are smoothed [53].

The PIV plus numerics combination has promoted the path toward predicting aneurysm rupture. Most research groups predict aneurysm rupture based on hemodynamical variables (mainly WSS or WSS-based) and morphological details [40]. While there is a debate on high WSS [54] or low WSS [55] as the causes of IA rupture, there is a consensus that complex flow patterns are present in the vast majority of ruptured IAs [40]. The results of the MATCH Challenge have shown that the groups with the best prediction for the aneurysm rupture require additional parameters such as the aneurysm site, details of the inflow jet, and vortices identification [40,41]. Recently, the analysis of vortical structures appearing in aneurysms has been considered very important for analyzing the IA rupture [56,57]. These structures and the impinging locations have only been measured in idealized aneurysms [58]. Therefore, an experimental analysis of the vortices inside a real aneurysm could shed light on rupture mechanisms.

Besides analyzing the vortices inside the aneurysm, incorporating fluid-structure interaction (FSI) models for better simulation accuracy is increasingly recognized, as it can be crucial in cardiovascular applications where the vessel deforms [59]. For example, Bazilevs et al. developed a dynamic mesh-based FSI model, allowing simulation of how blood flow interacts with moving or flexible vessel walls. The ability to model real-time geometry changes significantly improves hemodynamic and wall stress predictions [60]. Similarly, De Zelicourt et al. applied dynamic mesh strategies to capture unsteady flow characteristics and vessel deformation, confirming the importance of considering moving boundaries, especially in geometries experiencing significant flow variations [61]. Additionally, Cheng et al. demonstrated that employing a dynamic mesh for CFD simulations allows for the accurate resolution of flow patterns and geometric changes in ruptured and unruptured intracranial aneurysms. This method is effective for studying how changes in aneurysm shape impact flow and wall shear stress, which are critical factors in the risk of aneurysm rupture [62]. These stress distributions are also modified if the vessel thickness is heterogeneous [63,64], as it also happens in abdominal aortic aneurysms [65,66]. Micro CT scans of resected tissue samples can provide useful information as stresses peak at the rupture site [67]. Nevertheless, the limited resolution of current imaging techniques does not allow the intracranial aneurysm vessel wall reconstruction in vivo. Moreover, there is an association between the wall motion and the risk of rupture [68]. Wall motion is complex to record as high spatial and temporal resolutions are required. Luckily, the 3D rotational angiography and 4D CTA techniques promise improvements in this area [59,68,69]. Therefore, wall modeling and inclusion in FSI simulations is also an active research area [70,71].

In the present work, we have focused on the experimental analysis of the movement inside a patient-specific aneurysm. We have employed in vitro high-speed particle tracking velocimetry (PTV) to capture the flow evolution. An aneurysm model has been constructed from patient medical images to visualize the aneurysm's inner structures during the cardiac cycle. To this end, a blood-mimicking fluid seeded with particles has been employed. Finally, trajectories have been obtained by processing the experimental videos. All the experimental results have been compared with the numerical simulations. This numerical study has been extended to the temporal analysis of that patient and two additional ones where WSS-based variables have been obtained.

2. Materials and methods

2.1. Geometry

Three patients with diagnosed aneurysms were included in this

study. CT scanned them at the University Hospital of Badajoz (Fig. 1). The data included in this study was accessed during May and July 2023 and the researchers did not have access to any information that could identify individual participants.

The location of the aneurysm of the first patient is at the point where Middle Cerebral Artery (MCA) and Anterior Cerebral Artery (ACA) bifurcate from the Internal Carotid Artery (ICA). The second and third patients have developed an aneurysm at the Basilar Artery (BA) bifurcation into the Posterior Cerebral Arteries (PCA). Their main measurements are detailed in Table 1.

The 3D Slicer software was used to import digital imaging and communications in medicine images, also known as DICOM images [72]. Then, a four-step manual segmentation procedure was conducted: (i) Two intensity thresholds (130 HU and 335 HU) were applied to the first image of the patient to select the pixels belonging to the area of interest, (ii) by applying a similar interval to the rest of the images the targeted region undergone a growing process, (iii) additional pixels not automatically selected in step (i) and according to a radiologist criterion, were manually included to the previous region, and (iv) other adjacent vessels connected to the geometry of interest were removed. In this way, it was acquired a 3D model and geometry. Additionally, we applied wrapping and smoothing processes to this geometry. The final result was exported in STL to start the model manufacturing and the numerical computing.

Table 1
Hydraulic diameters of the aneurysm's arteries. Dome length accounts for the maximum elongation within the dome.

Patient 1	Length (mm)	Patient 2	Length (mm)	Patient 3	Length (mm)
ICA	3.78	**Left PCA**	1.38	**Left PCA**	0.80
ACA	2.25	**Right PCA**	1.49	**Right PCA**	1.32
MCA	2.47	**BA**	2.16	**BA**	2.16
Dome	8.50	**Dome**	6.10	**Dome**	4.70

2.2. Numerical method

This section introduces the numerical method followed in the present study. A steady-state numerical simulation was conducted for patient one and was experimentally validated. Subsequently, a transient numerical study was performed for all three patients.

2.2.1. Fluid

Using a Newtonian fluid instead of a non-Newtonian one influences the simulation results [57]. Nevertheless, this influence on the velocity can be negligible [12] or overcome depending on the solver's election [53]. We selected three instants in the cardiac cycle to check the non-Newtonian behavior for patient one: systole, intermediate instant, and diastole. The calculated shear rates were: 177.25 s^{-1}, 132.30 $s^{-1,}$ and 82.00 s^{-1}, respectively. Consequently, the blood viscosity for shear rates were: 3.90 mPas, 4.1 mPas, and 5.00 mPas, respectively. Therefore, a Newtonian assumption is justified as the viscosity does not change in >50 % of the cycle. A blood-mimicking fluid ($\rho_f = 1072\ kg/m^3$, $\mu = 3.15 \times 10^{-3}$ Pa s) was employed.

2.2.2. Boundary conditions

As the specific hemodynamic parameters were unavailable, a velocity profile from a similar aneurysm reported in the scientific literature [19] was selected as the boundary condition for the ICA. The selected points (systole, intermediate, and diastole) corresponded to different Reynolds numbers (*Re*), i.e., $Re = 395$, $Re = 857$, and $Re = 639$ (see Fig. 2, left). As we are interested in studying the onset of vortex initiation, two more *Re* with lower values (11 and 150) were also included. Although these additional points correspond to flow rates lower than physiological ones, the absence of vortices facilitated the particle selection to improve the experimental visualization. Preliminary experiments were performed in the patient1′s geometry to obtain the outflow boundary conditions. We variated inlet flow rates for each branch. We calculated the flow percentage that circulates through MCA, 49 %, and the ACA, 51 %. The same flow rate percentage circulates through PCA for patients 2 and 3. The rigid wall assumption and the non-slip boundary conditions were also considered. The transient profiles used in the simulations are represented in Fig. 2. Regarding patients 2 and 3, a BA velocity profile was also taken from the scientific literature [72].

Considering the maximum velocity of the transient velocity profiles of Fig. 2, the maximum *Re* number for this simulation was estimated. The corresponding value is 952. In this case, the flow was assumed to be laminar, as this value is well within the laminar flow regime, which typically occurs for *Re* values below 2000.

2.2.3. Mesh and numerical parameters

The geometries of the aneurysms were discretized using an automatic algorithm, resulting in tetrahedrons with a size of 0.15 mm.

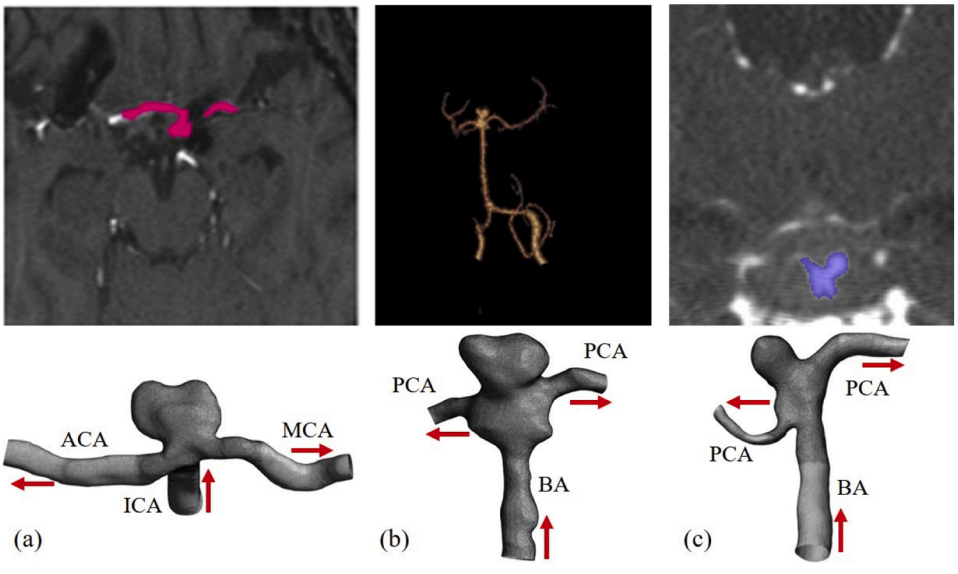

Fig. 1. Aneurysm medical images (top row) and acquired 3D mesh after segmentation and meshing (bottom row). Arrows indicate the movement direction.

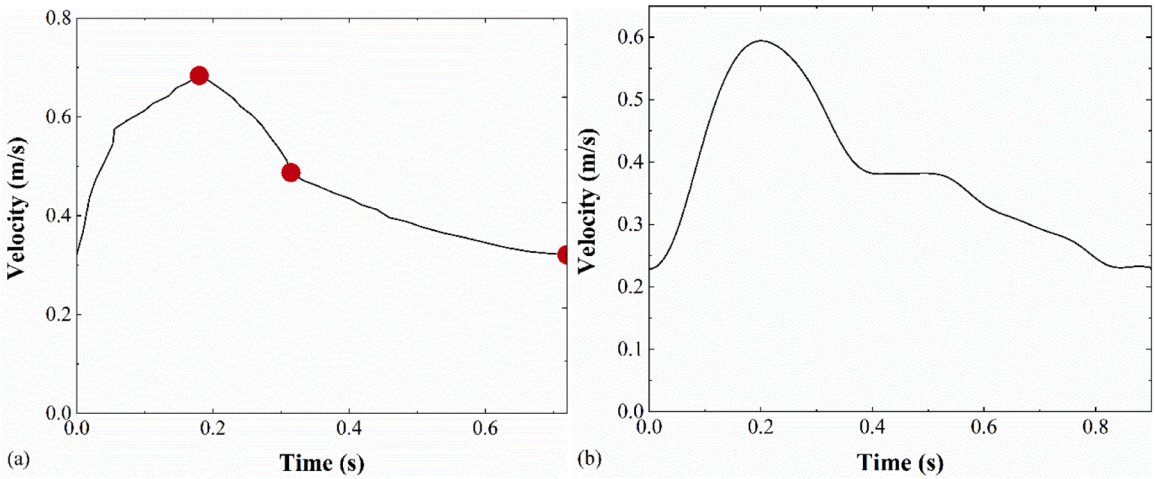

Fig. 2. Velocity profile imposed at the inlet for the transient simulations. (a) Patient 1; (b) Patient 2 and 3. The red points in the left figure correspond to systole, intermediate, and diastole flow rates, respectively.

Meshes statistics are shown in Table 2.

For the mesh convergence study, we halved (~1.2 Million elements) and doubled (~6.0 Million elements) the elements of the patient 1 mesh. Outlet pressures were monitored in every mesh to assess convergence. Table 3 shows the results of this study.

In this sense, as the difference is minimum between the results of Mesh B and Mesh C, and the computational effort is considerably more for mesh C, Mesh B was selected for the numerical studies. Following this logic and because the geometries of the other patients and boundary conditions are similar, the same mesh size was employed for the 3 patients.

The commercial software Fluent [74] was employed to solve the Navier-Stokes (NS) equations employing the finite volume method [75]. The equations were solved in both steady (ICA aneurysm) and unsteady (ICA/BA aneurysms) incompressible regimes. The pressure-based solver and the hydrodynamic equations have been combined. The Least Squares Cell Based algorithm was used to calculate the gradients in the cell centers. A second-order spatial discretization was employed for the pressure equation. An upwind approximation of the same order was used to perform the momentum equation spatial discretization. The velocity and pressure were coupled by using the SIMPLE procedure. A time-step of 0.001 s was considered for the transient simulations. This ensured that the Courant number stayed below 1. The pressure outlet result was nearly the same when the time step was divided by two. Three cardiac cycles were simulated to reach a quasi-periodic regime. The results of the last obtained cycle are just shown.

2.3. Experimental method

Due to its unique features, including transparency, flexibility, and biocompatibility, PDMS is a commonly used polymer to fabricate devices at both macro [73,76,77] and micro [77,78] scale levels. As a result, a PDMS biomodel was created in this study combining rapid prototyping and casting (lost core) [44] (see Fig. 3). Its refractive index is 1.41. It must be matched to prevent optical distortions [54]. Therefore, the present work employed a 52 % solution of dimethyl sulfoxide (DMSO) in water.

Table 2
Mesh parameters.

	Elements	Nodes	Avg. Sknewness
Patient 1	2455211	458598	0.22
Patient 2	3703615	673350	0.21
Patient 3	3676812	685207	0.22

Table 3
Mesh convergence study results.

Mesh	Elements	Avg. Pressure Outlet ACA (Pa)	% deviation	Avg. Pressure Outlet MCA (Pa	% deviation
A	1210128	−50.58	−10.58 %	−265.98	6.77 %
B	2455211	−44.02	3.76 %	−279.58	2.01 %
C	5980235	−45.74	0 %	−285.32	0 %

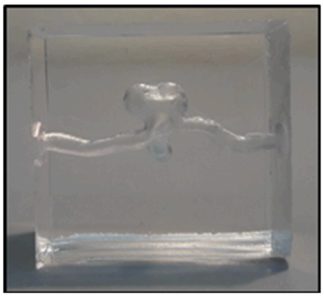

Fig. 3. PDMS aneurysm biomodel (patient 1) was manufactured using rapid prototyping and a lost core casting process.

A refractometer (Abbemat 500) measured the refractive indexes of both fluids and PDMS. Additionally, by using a densimeter (Anton Paar DMA 5000 M) and a typical Cannon–Feske viscosimeter, we obtained both fluid absolute density and viscosity at 25 °C (1072 kg/m^3, 3.15 × 10^{-3} Pas, respectively). It is worth mentioning that these values mimic the human blood ones under high shear rates, where the absolute density has a value of about 1060 kg/m^3 and dynamic viscosity has a value of about 4 × 10^{-3} Pas [55]. To visualize the fluid trajectories, polymethyl methacrylate (PMMA) particles with an average size of 60 μm were added to the fluid at a concentration of 100 ppm. Stokes's number was calculated to test the fidelity of the particles to the fluid trajectories. As the density of the particles, ρ_p (1200 kg/m^3), is comparable to the fluid, we have employed the expression $\frac{d_p^2(\rho_p - \rho_f)}{18\mu}\frac{v_f}{L_f}$, where d_p accounts for the particle diameter, and v_f and L_f are characteristic velocities and hydraulic diameter. If the worst possible conditions are selected, i.e., maximum flow rate and minimum hydraulic diameter within the geometry, Stokes's number is 0.0045. As this value is much lower than 0.1, particles do not interfere with the fluid movement, and their trajectories match the fluid ones with a negligible error. We checked the trajectories

observed for 60 μm particles by repeating the experiments (Re=11 and Re=150) using 20 μm particles, and the result was the same. Therefore, as the bigger particles were easier to visualize, they were employed in all experiments.

Fig. 4 shows the experimental setup. A tank with adjustable pressure is joined to a Büchner flask containing the blood-mimicking fluid. A magnetic mixer continuously worked during the tests to prevent the particles from settling down. The flow rate of the fluid leaving the flask was controlled by employing a liquid control valve. This liquid was pumped into the aneurysm model (see Fig. 5), where two additional control valves controlled the liquid flow through MCA and ACA. The control valves were located far downstream of each vessel to prevent introducing unnecessary fluctuations in the flow through the model.

By employing the ultra-high-speed recording capabilities of CMOS Photron FASTCAM SA5 camera, a group of 1024 × 1024 pixels images were recorded. The frame rate range (4000 fps to 7000 fps) was adjusted as a function of the flow rate to track the particles inside the blood-mimicking fluid. The exposure time (142.6 μs) was also adjusted to fix the light intensity. An optical zoom lens system allowed a variable magnification to observe the particles properly. These particles were focused by shifting the camera with a triaxial translation stage. Fig. 5 shows in detail all the equipment included in the setup. This equipment was placed on an optical table to control any movement. This table was placed on a pneumatic frame to prevent vibrations from the building or the researchers close to the table.

This setup's central part was adjusted to obtain zenithal pictures (Fig. 5). The diffuser and the optical fiber were positioned beneath the biomodel. A mirror (Q) placed above the biomodel and inclined 45° allowed the visualization of an additional plane orthogonal to the previous one. This plane contains a section of the aneurysm dome.

Before each experiment starts, the pressure in the tank (A) is adjusted by the valve (B) and the differential pressure meter (C). This pressure sets the flow rate at ICA. This flow rate is the sum of each outlet. Those flow rates were determined using two beakers and scales (I). Once the targeted flow rates were achieved, the following experimental procedure was conducted: 1) keep the pressure in the tank; 2) open the valve; 3) wait for 15 s to allow the flow to stabilize; and 4) record an image set at the previously mentioned frame rates.

A subset of 400 images for the two smallest flow velocities and 800 images for the rest were processed by ImageJ software [79]. The Z-projection method at the lowest intensity allowed us to get the pathlines. These pathlines were subsequently compared with the numerically obtained ones.

3. Results and discussion

3.1. Steady regime

To facilitate the description of the flow in the aneurysm, Fig. 6 illustrates a frontal and a top image. The inlet artery section is divided into three sections to assist with the flow analysis. However, only the top and bottom sectors are considered when analyzing the flow rates covering the onset of vortex appearance, as no significant motion is associated with the intermediate part.

3.1.1. Vortex appearance flow rates

As mentioned, two additional points were selected to examine particle trajectories without vortices. The flow rate corresponding to the minimum one during the cardiac cycle (diastole) was reduced to avoid vortexes within the aneurysm (Re=11, Fig. 7a).

Subsequently, the flow rate was increased until the vortex appeared when Re reached 150 (Fig. 7b). As observed, both numerical predictions and experiments coincide. In Fig. 7a, the flow behavior varies depending on the section of the ICA. Part of the top section flow (red in Fig. 7a) enters the aneurysm, diverting through the MCA without contacting the aneurysm dome or front wall (Fig. 6). Consequently, the lack of flow impingement and the fluid trajectories far away from the wall do not indicate a pressure increase on the surface. Conversely, the remaining liquid flowing through the upper sector and the liquid passing through the lower section of the ICA does not reach the aneurysm; instead, it diverts through ACA and the MCA.

Distinct behavior is observed at a higher flow rate (Fig. 7b). The flow in the lower section of the ICA primarily diverts through the ACA. A drastic change in the flow morphology is observed when entering the aneurysm through the top part. A toroidal vortex and a regular recirculation cell appear in the dome [54]. The vortex is generated by the part of the flow that does not impinge on the wall. Conversely, the flow impinging on the frontal wall creates a cell by ascending this wall and redirecting itself to MCA.

3.1.2. Physiological flows

As mentioned in the previous section, three different flow rates were selected for the ICA within the physiological ones for a patient suffering an IA in the same position as patient 1 [19]. Fig. 8 illustrates the results obtained during diastole. In diastole, the flow rate sharply increases with respect to the one when the vortex start appearing (Re=395 instead of 150). Consequently, the amount of flow that enters the dome increases.

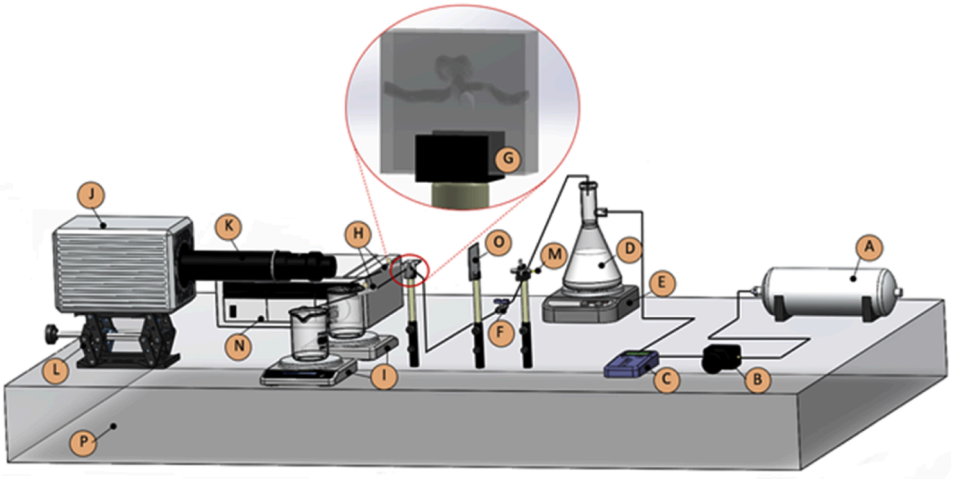

Fig. 4. Detail of the experimental setup: 2 l tank (A), valve (B), differential pressure meter (C), Büchner flask (D), magnetic stirrer (E), hydraulic control valve (F), aneurysm model (G), hydraulic control valves (H), beakers and weighing scales (I), ultra-high-speed camera (J); optical lenses (K), triaxial translation stage (L), optical fiber (M), illumination system (N), frosted glass diffuser (O) and optical table (P).

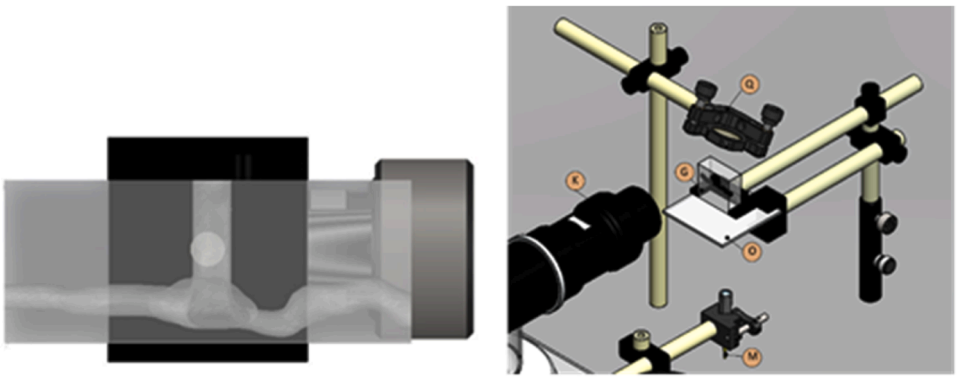

Fig. 5. Left: Aneurysm top view. Right: Experimental setup for top view shots.

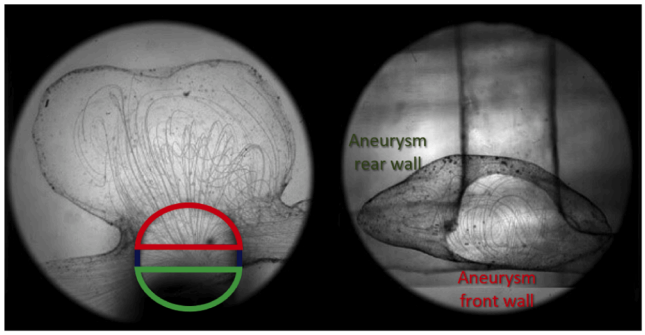

Fig. 6. Left: ICA sectors for flow analysis. Top (red), intermediate (navy), and bottom (green). Right: Aneurysm top view and detail of the ICA entrance.

Therefore, the pathlines extend to a more extensive region, including the top part of the dome. Moreover, the flow through the central region also enters the dome. Like previous cases, the liquid flowing through the lower region (green in Fig. 6) remains to divert itself through the exits. Another novelty with respect to previous cases, is the appearance of recirculation zones on the left and right sides of the dome.

As the flow rate increases for the central physiological case (Fig. 9), so does the area occupied by the streamlines. However, the overall structure remains similar to the diastolic case. Fig. 9 front view shows a higher concentration of vortices in the central region. Those vortices also approach the top part of the dome.

Finally, Fig. 10 shows the case with the biggest flow rate (Re=857). This case follows the same tendency as the previous ones, and the concentration of pathlines is increasing. The central part of the sac shows a bigger density of pathlines. Slow vortexes are noticeable on the left side. The vortices formed are located closer to the wall, which may have a relationship with the mechanism of rupture [56]. Varble et al. [56] have established a correlation between the hemodynamics and the morphology of ruptured IAs and vortex appearing and occupying large regions within the aneurysmal sac. The impingement on small regions in the wall can cause a pressure increase and can originate a rupture. In our case, the entering fluid impacts the front wall and quickly disperses. The structure formed by the trajectories can be classified as complex, as there are multiple recirculation cells [54]. The vortex structures observed in our simulations exhibit a noteworthy agreement with experimental findings. Figs. 7-10 demonstrate a close correspondence between the trajectories obtained from experiments and numerical simulations.

3.2. Transient regime

A streamlines velocity flow analysis can provide valuable insights into the flow patterns within an aneurysm.

Velocity gradients in the dome and neck of the aneurysm are essential for the endovascular treatment of IA [80]. Fig. 11 shows the streamlines plots illustrating the fluid flow patterns during the systole phase in the transient studies of aneurysms for the three patients. Fig. 12 represents them during the diastole phase.

For patient one, there is some fluid recirculation within the aneurysm, like in the steady simulation. The MCA has a higher outflow velocity, which can be justified by the size difference between this artery and the ACA (there is a minor stenosis at the MCA entrance). Aneurysm recirculation can also be observed in patients 2 and 3. However, there is a higher streamlines concentration for these aneurysms, likely related to the orientation of the arteries at the bifurcation. In other words, the aneurysms in the latter cases are directly aligned with the BA, unlike the ICA in patient one where the aneurysm plane is perpendicular to ICA axis. Again, there is significant fluid recirculation in the dome and the neck of the aneurysm. In the case of patient 3, there is a noticeable size difference in the PCA outlet arteries, causing the velocity in the left branch to be significantly higher than in the right branch in both the systole and diastole phases.

Regarding the flow in the outlet arteries, some recirculation is also observed, mainly in the MCA in patient 1, more pronounced during the systole phase. The same is visible in patient 3′s right PCA. Therefore, recirculation is enhanced due to local features in the geometry.

Vorticity is a vectorial quantity representing the local rotation of fluid particles within a flow field. It provides valuable insights into the flow patterns and mechanical stresses within the aneurysm sac and its surrounding blood vessels. Vorticity can provide a clear visual indication of vortex structures, flow separation, and areas of intense swirling motion. These patterns can help identify disturbed or abnormal flow regions within an aneurysm. Endothelial cells are sensitive to those changes, and this complex pattern may contribute to the growth of the structures, wall degeneration, and, ultimately, their rupture [11].

Fig. 13 represents the vorticity profile at systole for the three studied cases. The highest vorticity values are reached for patients 1 and 3, with higher velocity magnitude. In the first case, a significant fluid particle rotation is present towards the bifurcation, neck, and outflow to the MCA. Vorticity values are generally higher in this branch compared to the ACA. In the case of patient 3, due to the velocity asymmetry in the PCA branches (Figs. 11 and 12), there is a noticeable difference in vorticity levels between the outlet arteries. For patient 2, there is a smaller difference between the left and right branches of the PCA, with higher vorticity in the left branch. Comparing the vorticity levels among the three aneurysms, it is noticeable that there are higher values in the dome region for patients 2 and 3 compared to patient 1. According to the experimental observations in patient 1, the flow through the ICA drastically decelerates because of the wall proximity. Then, part of it flows through ACA and MCA, and the rest ascends to hit the aneurysm dome.

Conversely, in patients 2 and 3, the flow goes straight through BA and impinges on the aneurysm dome. Therefore, a larger amount of fluid hits patients 2 and 3′s dome due to the geometric differences. It is also

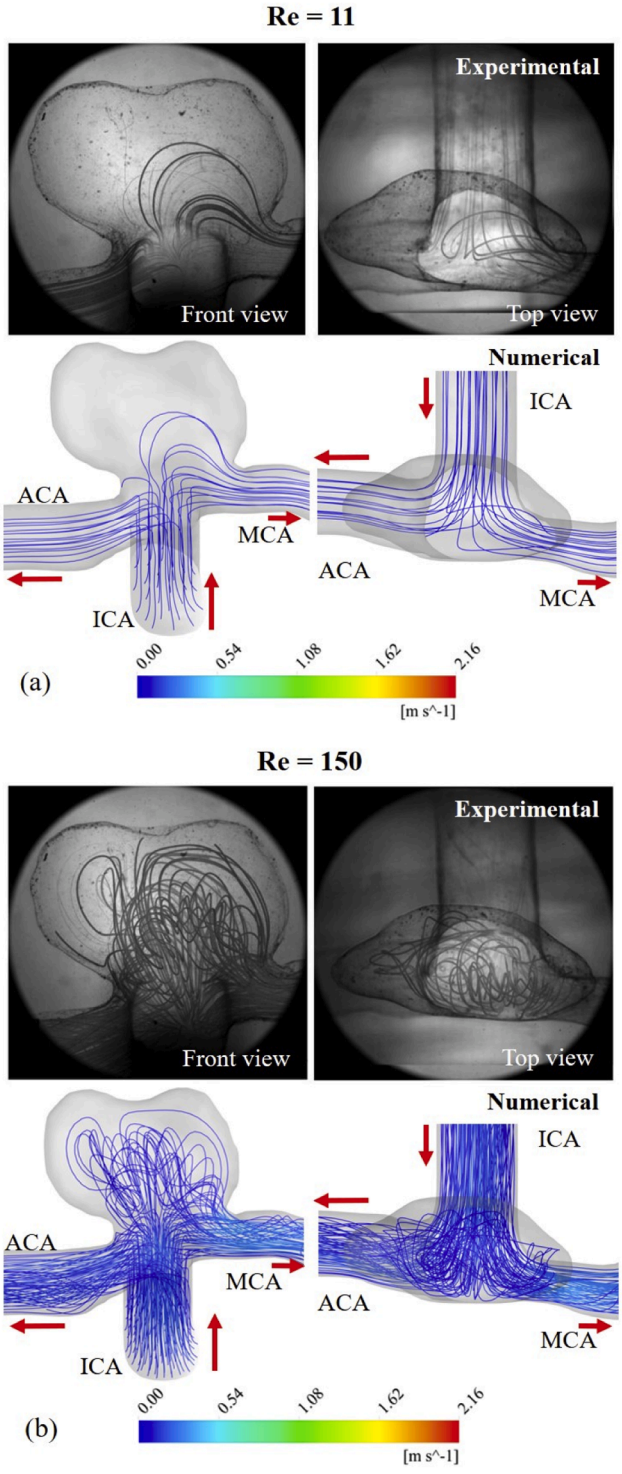

Fig. 7. Experimental and numerical results for minimum *Re*. Left: *Re* = 11; Right: *Re* = 150.

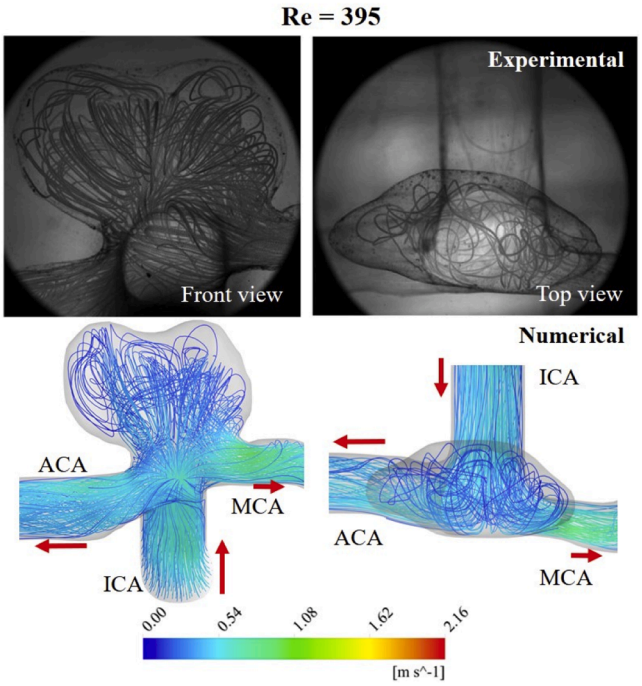

Fig. 8. Experimental and numerical results for diastole.

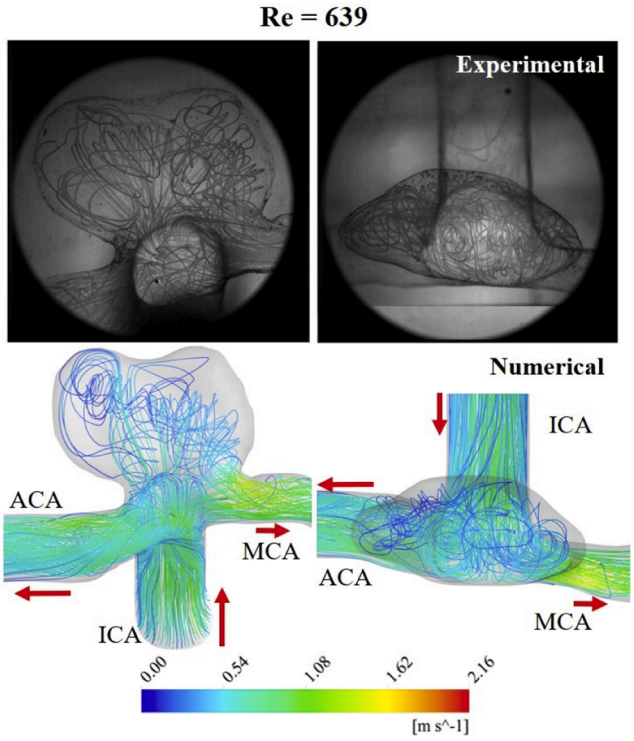

Fig. 9. Intermediate physiological flow results. Experimental trajectories (top row) vs simulations (bottom row).

noteworthy that there is a large blue zone in patient two before the bifurcation to the PCA arteries. This low-vorticity zone is related to the expansion of the fluid domain before the bifurcation, resulting in limited fluid motion in this region. On the other hand, there is a small constriction in the BA before that enlargement, where higher vorticity levels are observed, which is not as visible in the inlet arteries of patients 1 and 3, whose geometry is more uniform.

In aneurysm initiation and growth, prolonged exposure to low WSS levels can lead to endothelial dysfunction, a precursor to aneurysm formation [55]. As mentioned in the introduction, both low [55] and high WSS[54] magnitudes in localized regions can induce mechanical stress on the vessel walls, potentially leading to aneurysm rupture. WSS is also important to assess the effect on endothelial cells, as appropriate levels of WSS are necessary to maintain endothelial cell function and promote vascular health. Abnormal WSS patterns, such as low or oscillatory WSS, can disrupt the endothelial cell phenotype, impairing their

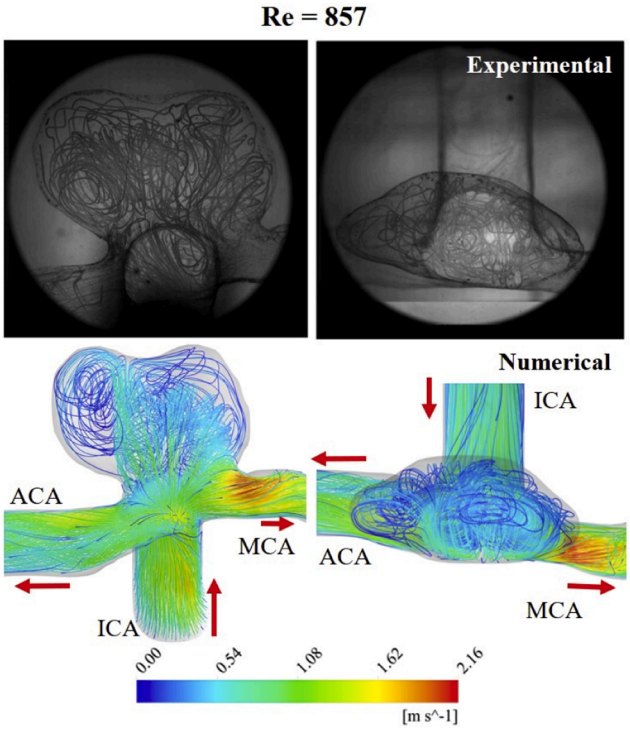

Fig. 10. Experimental and numerical results for highest (systole) flow rate.

ability to regulate vascular tone, inflammation, and thrombosis [11].

Fig. 14 displays the Time-Averaged Wall Shear Stress (TAWSS) plots for the three patients through the entire cardiac cycle.

TAWSS plots exhibit several similarities to the vorticity plots in the cases of study. In patient 1, a large velocity gradient is observed in the bifurcation zone, neck, and MCA, resulting in high WSS values throughout the cardiac cycle. There is also a small region in the ACA with higher TAWSS, with slight constriction and geometric deviation. In patient 2, TAWSS values are lower throughout the geometry, and no red zones (around 25 Pa) are observed. There are also very low TAWSS in the expansion before the bifurcation. TAWSS are higher in the left PCA compared to the right PCA. In patient 3, this difference between the branches is even more pronounced, significantly higher than the TAWSS in the left branch. It is also noticeable that in the dome of the aneurysm, TAWSS is higher in patients 2 and especially 3, compared to patient 1. This region of low TAWSS can be a potential rupture zone for patient 1 due to the continuous degeneration of the aneurysm wall [55].

Oscillatory Shear Index (OSI) and Relative Residence Time (RRT) are additional hemodynamic parameters that provide valuable information about the flow characteristics and their potential impact on the aneurysm wall. Their calculation is based on WSS values [81]. OSI quantifies the extent of flow oscillations and changes in direction within the aneurysm. OSI provides insights into the spatial distribution of disturbed flow patterns and identifies areas with low or oscillatory WSS. High OSI values are associated with regions of complex flow, flow impingement, and potential endothelial cell dysfunction. Elevated OSI correlates with aneurysm initiation, growth, and rupture [82]. RRT estimates the cumulative exposure of the aneurysm wall to blood flow over time. It provides insights into the local hemodynamic conditions that may contribute to aneurysm development and progression. High RRT values indicate prolonged residence time and potential blood stasis, which can trigger endothelial dysfunction, thrombosis, and inflammation [83].

Fig. 15a shows significant areas of recirculation for patient 1, particularly in the dome of the aneurysm and the posterior regions of the MCA and ACA. These regions also have a high particle residence (Fig. 16a). The pre-bifurcation enlargement (patient 2, Fig. 16b) creates favorable conditions for developing new aneurysms. This enlargement likely arises from weakness in the arterial wall due to these high residence areas [80]. The OSI plot and the streamlines confirm a significant recirculation (Fig. 11b and 15b). Conversely, patient 3 exhibits high OSI and RRT in the inflow artery (BA) instead of the aneurysm dome, as there is significant recirculation but also elevated WSS levels in this region. This difference may be related to the fact that aneurysm 3 is relatively smaller than the others.

Figs. 15 and 16 show that the regions where the aneurysms have a larger dimension, almost in a beak-like shape, are associated with higher RRT and OSI areas. The hemodynamic study of these two parameters is

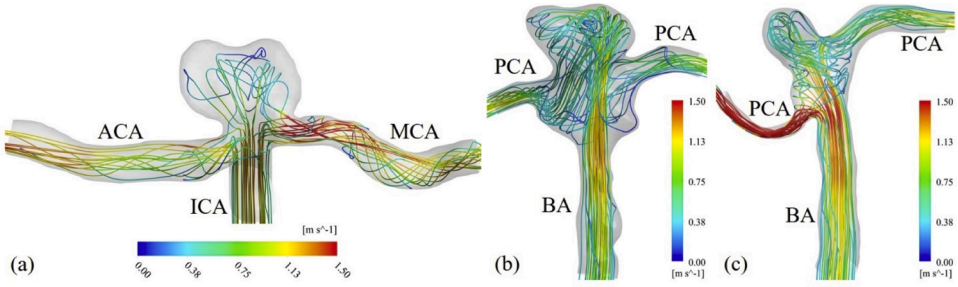

Fig. 11. Velocity streamlines at systole. (a) Patient 1; (b) Patient 2; (c) Patient 3.

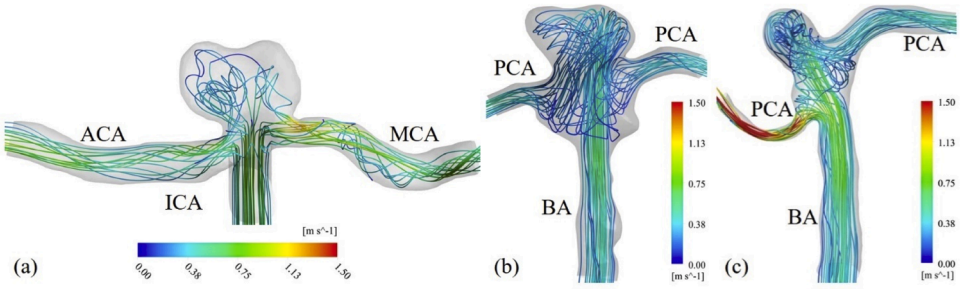

Fig. 12. Velocity streamlines at diastole. (a) Patient 1; (b) Patient 2; (c) Patient 3.

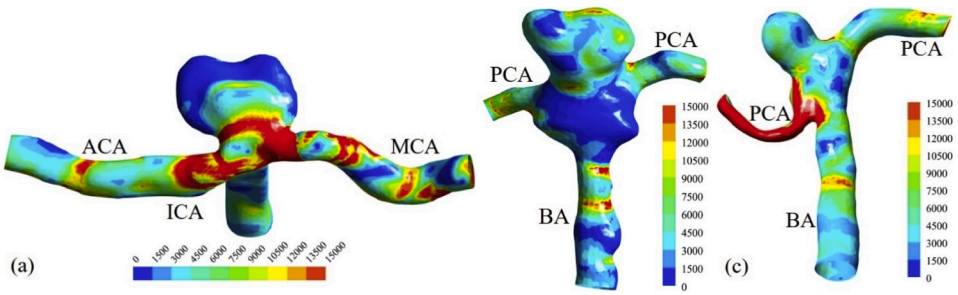

Fig. 13. Vorticity profiles at systole. (a) Patient 1; (b) Patient 2; (c) Patient 3.

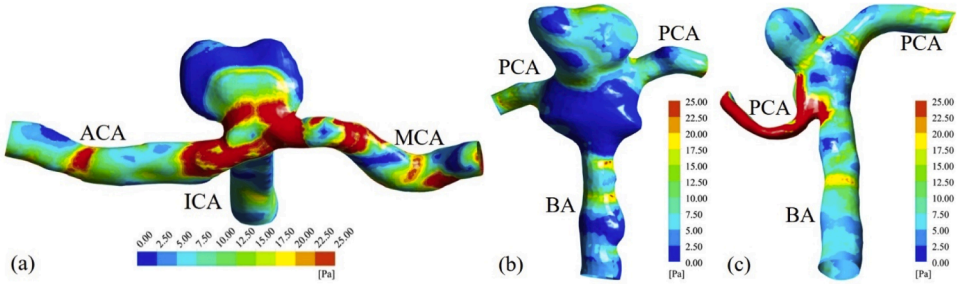

Fig. 14. TAWSS profiles. (a) Patient 1; (b) Patient 2; (c) Patient 3.

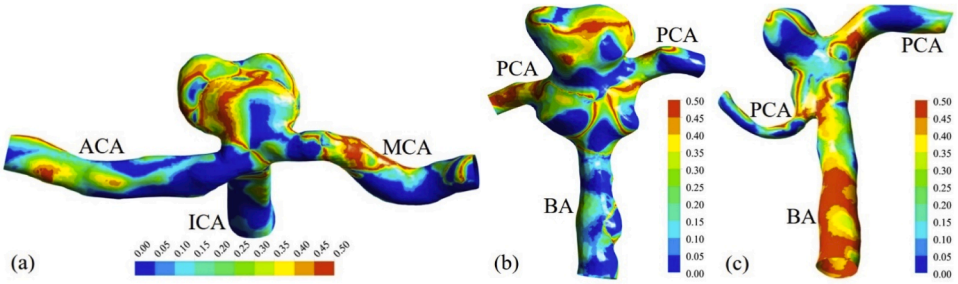

Fig. 15. OSI profiles. (a) Patient 1; (b) Patient 2; (c) Patient 3.

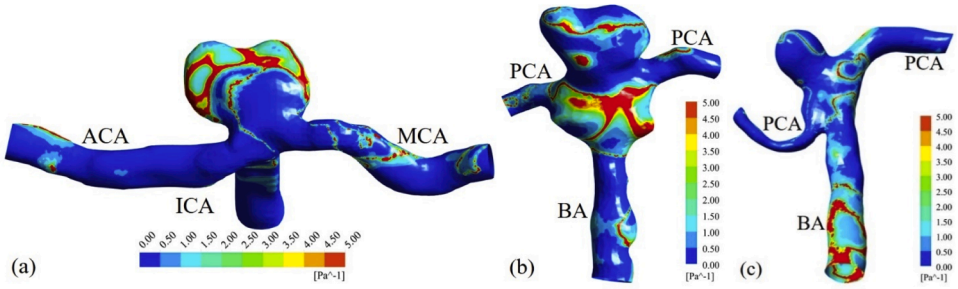

Fig. 16. RRT profiles. (a) Patient 1; (b) Patient 2; (c) Patient 3.

important to access these areas of potential arterial wall weakness and aid in developing effective treatments.

4. Conclusions

This study examined various flow rates for a steady case. Particle tracking velocimetry, applied to the experimental analysis of the flow inside a patient-specific aneurysm model, has allowed experimental validation of numerical simulation and a better understanding of the flow characteristics within the aneurysm for different flow rates. More straightforward trajectories can be observed when employing significantly reduced flow rates. The flow behavior changes drastically if the flow rate increases gradually from diastole to systole. Recirculation regions and vortex structures appear within the aneurysm. Moreover, jet impingement areas can be accurately localized.

Transient regime numerical studies during the systole and diastole phases revealed fluid recirculation within the aneurysm, higher outflow velocities in specific arteries, and distinct flow patterns depending on the patient and aneurysm location. Vorticity analysis highlighted areas of intense swirling motion, indicating the presence of vortex structures

and disturbed flow regions. The analysis demonstrated a correlation between the dimensions of the aneurysm and areas of high RRT and OSI, suggesting a relationship between hemodynamic parameters and arterial wall weakness. The use of CFD presents important advantages, particularly in the clinical context. First, its simplicity and lower computational cost make it a practical tool, allowing faster simulations and more efficient resource use for clinical applications where quick results are essential. Secondly, it does not require detailed mechanical properties of the aneurysm wall, such as elasticity and thickness, which are often unavailable in clinical settings. These findings have important implications for developing preventive measures and treatment strategies for intracranial aneurysms.

In summary, the comprehensive investigation of flow patterns and hemodynamic parameters within intracranial aneurysms has provided valuable insights into their behavior. Combining this experimental and numerical approach can be a perfect alternative to PIV. The PTV experimental learning curve is faster, more accessible, cost-effective, and requires reasonable processing time. This methodology can be extended to any morphology, non-Newtonian fluids, or transient studies. Future improvements in the manufacturing techniques will allow us to apply this technique in flexible aneurysms with heterogeneous walls. The knowledge extracted can contribute to improving treatment approaches that target specific flow characteristics and regions of arterial wall weakness, ultimately enhancing patient outcomes and reducing the risk of aneurysm rupture.

CRediT authorship contribution statement

A. Souza: Writing – review & editing, Writing – original draft, Visualization, Validation, Software, Methodology, Investigation, Formal analysis, Data curation. **D. Lopes:** Writing – review & editing, Writing – original draft, Software. **S. Souza:** Writing – original draft, Validation, Software, Investigation, Data curation. **J. Ribeiro:** Writing – review & editing, Supervision, Resources, Funding acquisition, Formal analysis, Conceptualization. **R.A. Lima:** Writing – review & editing, Supervision, Resources, Project administration, Investigation, Funding acquisition. **C. Ferrera:** Writing – review & editing, Writing – original draft, Visualization, Validation, Supervision, Project administration, Investigation, Formal analysis, Data curation, Conceptualization.

Declaration of competing interest

The authors declare that they have no known competing financial interests or personal relationships that could have appeared to influence the work reported in this paper.

Acknowledgments

C. Ferrera gratefully acknowledges funding from the Junta de Extremadura through grant IB20105 (partially funded by FEDER). The authors additionally acknowledge the projects EXPL/EME-EME/0732/2021 and 2022.06207.PTDC for the financial support, through national funds (OE), within the scope of the Scientific Research and Technological Development Projects (IC&DT) program in all scientific domains (PTDC), PORTUGAL 2020 Partnership Agreement, European Regional Development Fund (FEDER), via the Foundation for Science and Technology, I.P. (FCT, I.P) and the R&D Units projects UIDB/00690/2020, UIDB/04077/2020, UIDP/04077/2020, UIDB/04436/2020, UIDB/00532/2020 and LA/P/0045/2020. Andrews Souza acknowledges FCT for the Ph.D. scholarship 2021.07961.BD.

Data availability

No data was used for the research described in the article.

References

[1] G. B. D. 2016 C. of D. Collaborators, Global, regional, and national age-sex specific mortality for 264 causes of death, 1980-2016: a systematic analysis for the Global Burden of Disease Study 2016, Lancet 390 (10100) (Sep. 2017) 1151–1210, https://doi.org/10.1016/S0140-6736(17)32152-9.

[2] C. Rodriguez-Régent, et al., Non-invasive diagnosis of intracranial aneurysms, Diagn. Interv. ImAging 95 (12) (2014) 1163–1174, https://doi.org/10.1016/j.diii.2014.10.005.

[3] M.H.M. Vlak, A. Algra, R. Brandenburg, G.J.E. Rinkel, Prevalence of unruptured intracranial aneurysms, with emphasis on sex, age, comorbidity, country, and time period : a systematic review and meta-analysis, Lancet Neurol. 10 (7) (2011) 626–636, https://doi.org/10.1016/S1474-4422(11)70109-0.

[4] B.G. Thompson, et al., Guidelines for the Management of Patients With Unruptured Intracranial Aneurysms: a Guideline for Healthcare Professionals From the, American Heart Association/American Stroke Association 46 (8) (2015), https://doi.org/10.1161/STR.0000000000000070.

[5] P.S. Amenta, et al., Analysis of Nonmodifiable Risk Factors for Intracranial Aneurysm Rupture in a Large, Retrospective Cohort, Neurosurgery. 70 (3) (2011) 693–701, https://doi.org/10.1227/NEU.0b013e3182354d68.

[6] H. Henkes, W. Weber, The Past, Present and Future of Endovascular Aneurysm Treatment, Clin. Neuroradiol. 25 (2015) 317–324, https://doi.org/10.1007/s00062-015-0403-1.

[7] S. Schob, et al., Flow diversion beyond the circle of Willis: endovascular aneurysm treatment in peripheral cerebral arteries employing a novel low-profile flow diverting stent, J. Neurointerv. Surg. 11 (12) (2019) 1227–1234, https://doi.org/10.1136/neurintsurg-2019-014840.

[8] A. Malhotra, et al., Management of unruptured intracranial aneurysms in older adults: a cost-effectiveness analysis, Radiology. 291 (2) (2019) 411–417, https://doi.org/10.1148/radiol.2019182353.

[9] J.C. Lasheras, The Biomechanics of Arterial Aneurysms, Annual Review ofFluid Mechanics 39 (2007) 293–321, https://doi.org/10.1146/annurev.fluid.39.050905.110128.

[10] G. Tromp, S. Weinsheimer, A. Ronkainen, H. Kuivaniemi, Molecular basis and genetic predisposition to intracranial aneurysm, Ann. Med. 46 (8) (2014) 597–606, https://doi.org/10.3109/07853890.2014.949299.

[11] M.R. Levitt, et al., Genetic correlates of wall shear stress in a patient-specific 3D-printed cerebral aneurysm model, J. Neurointerv. Surg. 11 (10) (2019) 999–1003, https://doi.org/10.1136/neurintsurg-2018-014669.

[12] S.V. Frolov, S.V. Sindeev, D. Liepsch, A. Balasso, Experimental and CFD flow studies in an intracranial aneurysm model with Newtonian and non-Newtonian fluids, Technology and Health Care 24 (3) (2016) 317–333, https://doi.org/10.3233/THC-161132.

[13] S. Baratchi, K. Khoshmanesh, O.L. Woodman, S. Potocnik, K. Peter, P. McIntyre, Molecular Sensors of Blood Flow in Endothelial Cells, Trends. Mol. Med. 23 (9) (2017) 850–868, https://doi.org/10.1016/j.molmed.2017.07.007.

[14] P.R. Hoskins, P.V. Lawford, B.J. Doyle, Cardiovascular Biomechanics (2017), https://doi.org/10.1007/978-3-319-46407-7.

[15] J.R. Cebral, M. Raschi, Suggested connections between risk factors of intracranial aneurysms: a review, Ann. Biomed. Eng. 41 (7) (2013) 1366–1383, https://doi.org/10.1007/s10439-012-0723-0.

[16] P. Nair et al., "Hemodynamic characterization of geometric cerebral aneurysm templates," vol. 49, pp. 2118–2126, 2016, doi: 10.1016/j.jbiomech.2015.11.034.

[17] G. Zhou, Y. Zhu, Y. Yin, M. Su, M. Li, Association of wall shear stress with intracranial aneurysm rupture : systematic review and meta- analysis, Sci. Rep. 7 (2017) 1–8, https://doi.org/10.1038/s41598-017-05886-w.

[18] M.L. Bøthun, Ø.A. Haaland, N. Logallo, F. Svendsen, L. Thomassen, C.A. Helland, Cerebrovascular reactivity after treatment of unruptured intracranial aneurysms — A transcranial Doppler sonography and acetazolamide study, J. Neurol. Sci. 363 (2016) 97–103, https://doi.org/10.1016/j.jns.2015.12.024.

[19] M. Jahed, F. Ghalichi, M. Farhoudi, Comparison of blood velocity between Transcranial Doppler and numerical method in the patient-specific Circle of Willis with aneurysm, Biomed. Mater. Eng. 30 (4) (2019) 427–438, https://doi.org/10.3233/BME-191064.

[20] M.A. Basarab, D.A. Basarab, N.S. Konnova, D.D. Matsievskiy, V.A. Matveev, Analysis of chaotic and noise processes in a fluctuating blood flow using the Allan variance technique, Clin. Hemorheol. Microcirc. 64 (4) (2016) 921–930, https://doi.org/10.3233/CH-168011.

[21] P. Bouillot, et al., Robust cerebrovascular blood velocity and flow rate estimation from 4D-CTA, Med. Phys. 46 (5) (2019) 2126–2136, https://doi.org/10.1002/mp.13454.

[22] D. Brunozzi, P. Theiss, A. Andrews, S. Amin-Hanjani, F.T. Charbel, A. Alaraj, Correlation Between Laminar Wall Shear Stress and Growth of Unruptured Cerebral Aneurysms: in Vivo Assessment, World Neurosurg. 131 (2019) e599–e605, https://doi.org/10.1016/j.wneu.2019.08.005.

[23] J. Szajer, K. Ho-Shon, A comparison of 4D flow MRI-derived wall shear stress with computational fluid dynamics methods for intracranial aneurysms and carotid bifurcations — A review, Magn. Reson. ImAging 48 (2018) 62–69, https://doi.org/10.1016/j.mri.2017.12.005.

[24] C. Roloff, D. Stucht, O. Beuing, and P. Berg, "Comparison of intracranial aneurysm flow quantification techniques : standard PIV vs stereoscopic PIV vs tomographic PIV vs phase- contrast MRI vs CFD," pp. 1–8, 2018, doi: 10.1136/neurintsurg-2018-013921.

[25] M.C. Brindise, et al., Multi-modality cerebral aneurysm haemodynamic analysis: in vivo 4D flow MRI, in vitro volumetric particle velocimetry and in silico

computational fluid dynamics, J. R. Soc. Interface 16 (158) (2019), https://doi.org/10.1098/rsif.2019.0465.
[26] O. Amili, J. Golzarian, F. Coletti, In Vitro Study of Particle Transport in Successively Bifurcating Vessels, Ann. Biomed. Eng. 47 (11) (2019) 2271–2283, https://doi.org/10.1007/s10439-019-02293-2.
[27] M.H. Friedman, L.W. Ehrlich, Numerical simulation of aortic bifurcation flows: the effect of flow divider curvature, J. Biomech. 17 (12) (1984), https://doi.org/10.1016/0021-9290(84)90001-0.
[28] A.C. Burleson, C.M. Strother, V.T. Turitto, Computer Modeling of Intracranial Saccular and Lateral Aneurysms for the Study of Their Hemodynamics, Neurosurgery. 37 (4) (Oct. 1995) 774–784, https://doi.org/10.1227/00006123-199510000-00023.
[29] J. Mikhal, B. Geurts, Immersed boundary method for pulsatile transitional flow in realistic cerebral aneurysms, Comput. Fluids. 91 (2014) 144–163, https://doi.org/10.1016/j.compfluid.2013.12.009.
[30] D.A. Steinman, J.S. Milner, C.J. Norley, S.P. Lownie, D.W. Holdsworth, Image-based computational simulation of flow dynamics in a giant intracranial aneurysm, American Journal of Neuroradiology 24 (4) (2003) 559–566.
[31] T. Hassan, et al., Hemodynamic analysis of an adult vein of Galen aneurysm malformation by use of 3D image-based computational fluid dynamics, American Journal of Neuroradiology 24 (6) (2003) 1075–1082.
[32] T. Hassan, et al., Computational replicas: anatomic reconstructions of cerebral vessels as volume numerical grids at three-dimensional angiography, American Journal of Neuroradiology 25 (8) (2004) 1356–1365.
[33] I.L. Oliveira, P. Cardiff, C.E. Baccin, J.L. Gasche, A numerical investigation of the mechanics of intracranial aneurysms walls: assessing the influence of tissue hyperelastic laws and heterogeneous properties on the stress and stretch fields, J. Mech. Behav. Biomed. Mater. 136 (Dec. 2022), https://doi.org/10.1016/j.jmbbm.2022.105498.
[34] S. Saalfeld, S. Voß, O. Beuing, B. Preim, P. Berg, Flow-splitting-based computation of outlet boundary conditions for improved cerebrovascular simulation in multiple intracranial aneurysms, Int. J. Comput. Assist. Radiol. Surg. 14 (10) (2019) 1805–1813, https://doi.org/10.1007/s11548-019-02036-7.
[35] J.E. Hippelheuser, A. Lauric, A.D. Cohen, A.M. Malek, Realistic non-Newtonian viscosity modelling highlights hemodynamic differences between intracranial aneurysms with and without surface blebs, J. Biomech. 47 (15) (2014) 3695–3703, https://doi.org/10.1016/j.jbiomech.2014.09.027.
[36] E.L. Leemans, et al., Impact of Intracranial Aneurysm Morphology and Rupture Status on the Particle Residence Time, Journal of Neuroimaging 29 (4) (2019) 487–492, https://doi.org/10.1111/jon.12618.
[37] T. Otani, S. Ii, T. Shigematsu T., et al., Computational study for the effects of coil configuration on blood flow characteristics in coil-embolized cerebral aneurysm, Med. Biol. Eng. Comput. 55 (2017) 697–710, https://doi.org/10.1007/s11517-016-1541-6.
[38] H. Yadollahi-Farsani, E. Scougal, M. Herrmann, W. Wei, D. Frakes, B. Chong, Numerical study of hemodynamics in brain aneurysms treated with flow diverter stents using porous medium theory, Comput. Methods Biomech. Biomed. Engin. 22 (11) (2019) 961–971, https://doi.org/10.1080/10255842.2019.1609457.
[39] Y. Li, D.I. Verrelli, W. Yang, Y. Qian, W. Chong, A pilot validation of CFD model results against PIV observations of haemodynamics in intracranial aneurysms treated with flow-diverting stents, J. Biomech. (2019) 109590, https://doi.org/10.1016/j.jbiomech.2019.109590.
[40] P. Berg, et al., Multiple Aneurysms AnaTomy CHallenge 2018 (MATCH)—Phase II: rupture risk assessment, Int. J. Comput. Assist. Radiol. Surg. 14 (10) (2019) 1795–1804, https://doi.org/10.1007/s11548-019-01986-2.
[41] P. Berg, S. Saalfeld, S. Voß, O. Beuing, G. Janiga, A review on the reliability of hemodynamic modeling in intracranial aneurysms: why computational fluid dynamics alone cannot solve the equation, Neurosurg. Focus. 47 (1) (2019) 1–9, https://doi.org/10.3171/2019.4.FOCUS19181.
[42] G.G. Ferguson, Physical factors in the initiation, growth, and rupture of human intracranial saccular aneurysms, J. Neurosurg. 37 (6) (1972) 666–677, https://doi.org/10.3171/jns.1972.37.6.0666.
[43] H.J. Steiger, D.W. Liepsch, A. Poll, H.J. Reulen, Hemodynamic stress in terminal saccular aneurysms: a laser-doppler study, Heart Vessels 4 (3) (1988) 162–169, https://doi.org/10.1007/BF02058429.
[44] A. Souza, et al., 3D manufacturing of intracranial aneurysm biomodels for flow visualizations: low cost fabrication processes, Mech. Res. Commun. 107 (2020) 103535, https://doi.org/10.1016/j.mechrescom.2020.103535.
[45] V. Keshav, et al., Reconstructing patient-specific cerebral aneurysm vasculature for in vitro investigations and treatment efficacy assessments, Journal of Clinical Neuroscience 61 (2019) 153–159, https://doi.org/10.1016/j.jocn.2018.10.103.
[46] Y. Li, D.I. Verrelli, W. Yang, Y. Qian, W. Chong, A pilot validation of CFD model results against PIV observations of haemodynamics in intracranial aneurysms treated with flow-diverting stents, J. Biomech. 100 (2020) 109590, https://doi.org/10.1016/j.jbiomech.2019.109590.
[47] L. Xu, M. Sugawara, G. Tanaka, M. Ohta, H. Liu, R. Yamaguchi, Effect of elasticity on wall shear stress inside cerebral aneurysm at anterior cerebral artery, Technology and Health Care 24 (3) (2016) 349–357, https://doi.org/10.3233/THC-161135.
[48] M. Matsuura, S. Tupin, M. Ohta, Compliance effect on the flow condition in vascular in vitro experiments, in: ASME International Mechanical Engineering Congress and Exposition, Proceedings (IMECE) 3, 2018, pp. 1–7, https://doi.org/10.1115/IMECE201887362.
[49] F. Gaidzik, D. Stucht, C. Roloff, O. Speck, D. Thévenin, G. Janiga, Transient flow prediction in an idealized aneurysm geometry using data assimilation, Comput. Biol. Med. 115 (2019), https://doi.org/10.1016/j.compbiomed.2019.103507.
[50] A.Y. Usmani, K. Muralidhar, Flow in an intracranial aneurysm model: effect of parent artery orientation, J. Vis. (Tokyo) 21 (5) (2018) 795–818, https://doi.org/10.1007/s12650-018-0491-5.
[51] S.M. Rothenberger, et al., Modeling Bias Error in 4D Flow MRI Velocity Measurements, IEEe Trans. Med. ImAging 41 (7) (2022) 1802–1812, https://doi.org/10.1109/TMI.2022.3149421.
[52] J. Zhang, S.M. Rothenberger, M.C. Brindise, M. Markl, V.L. Rayz, P.P. Vlachos, Wall Shear Stress Estimation for 4D Flow MRI Using Navier–Stokes Equation Correction, Ann. Biomed. Eng. 50 (12) (2022) 1810–1825, https://doi.org/10.1007/s10439-022-02993-2.
[53] D. Schanz, S. Gesemann, A. Schröder, Shake-The-Box: lagrangian particle tracking at high particle image densities, Exp. Fluids. 57 (5) (2016) 1–27, https://doi.org/10.1007/s00348-016-2157-1.
[54] J.R. Cebral, F. Mut, J. Weir, C.M. Putman, Association of hemodynamic characteristics and cerebral aneurysm rupture, American Journal of Neuroradiology 32 (2) (2011) 264–270, https://doi.org/10.3174/ajnr.A2274.
[55] J. Xiang, et al., Hemodynamic-morphologic discriminants for intracranial aneurysm rupture, Stroke 42 (1) (2011) 144–152, https://doi.org/10.1161/STROKEAHA.110.592923.
[56] N. Varble, G. Trylesinski, J. Xiang, K. Snyder, H. Meng, Identification of vortex structures in a cohort of 204 intracranial aneurysms, J. R. Soc. Interface 14 (130) (2017), https://doi.org/10.1098/rsif.2017.0021.
[57] K.M. Saqr, et al., What does computational fluid dynamics tell us about intracranial aneurysms? A meta-analysis and critical review, Journal of Cerebral Blood Flow and Metabolism 40 (5) (2019) 1021–1039, https://doi.org/10.1177/0271678X19854640.
[58] P. Yu, V. Durgesh, Experimental study of flow structure impact on the fluid parameters in saccular aneurysm models, Exp. Therm. Fluid. Sci. 138 (May) (2022) 110675, https://doi.org/10.1016/j.expthermflusci.2022.110675.
[59] A. Goetz, P. Jeken-Rico, Y. Chau, J. Sédat, A. Larcher, E. Hachem, Analysis of intracranial aneurysm haemodynamics altered by wall movement, Bioengineering 11 (3) (2024) 269, https://doi.org/10.3390/bioengineering11030269.
[60] Y. Bazilevs, M.-C. Hsu, D.J. Benson, S. Sankaran, A.L. Marsden, Computational fluid–structure interaction: methods and application to a total cavopulmonary connection, Comput. Biol. Med. 45 (1) (2010) 77–89, https://doi.org/10.1016/j.compbiomed.2008.09.006.
[61] D. De Zelicourt, K. Pekkan, H. Kitajima, D. Frakes, J. Parks, et al., Design and validation of a novel passive flow control concept for total cavopulmonary connection, J. Biomech. 38 (11) (2005) 2505–2514, https://doi.org/10.1016/j.jbiomech.2005.01.005.
[62] Z. Cheng, N.B. Wood, R.G. Gibbs, M. Bourne, X.Y. Xu, Geometric and flow features of ruptured and unruptured intracranial aneurysms: a comparative study, J. Biomech. 43 (16) (2010) 2793–2799, https://doi.org/10.1016/j.jbiomech.2010.07.018.
[63] R. Torii, M. Oshima, T. Kobayashi, K. Takagi, T. Tezduyar, Influence of wall thickness on fluid-structure interaction computations of cerebral aneurysms, Int J Numer Methods Biomed Eng 26 (2010) 336–347, https://doi.org/10.1002/cnm.1289.
[64] I. Oliveira, J.L. Gasche, J. Militzer, C. Baccin, P. Cardiff, On the influence of wall thickness heterogeneity in the mechanics of intracranial aneurysms, in: Proceedings of the ABCM International Congress of Mechanical Engineering (COBEM), 2021, https://doi.org/10.26678/ABCM.COBEM2021.COB2021-0451.
[65] E. Finol, S. Raut, A. Jana, V. de Oliveira, S. Muluk, The importance of patient-specific regionally varying wall thickness in abdominal aortic aneurysm biomechanics, J. Biomech. Eng. 135 (2013), https://doi.org/10.1115/1.4024578.
[66] C. Scotti, A. Shkolnik, S. Muluk, E. Finol, Fluid-structure interaction in abdominal aortic aneurysms: effects of asymmetry and wall thickness, Biomed. Eng. Online 4 (2005) 64, https://doi.org/10.1186/1475-925X-4-64.
[67] S. Voß, S. Saalfeld, T. Hoffmann, O. Beuing, S. Weigand, K. Jachau, et al., Fluid-structure simulations of a ruptured intracranial aneurysm: constant versus patient-specific wall thickness, Comput. Math. Methods Med. 2016 (2016) 1–8, https://doi.org/10.1155/2016/9854539.
[68] A.E. Vanrossomme, O.F. Eker, J.P. Thiran, G.P. Courbebaisse, K.Z. Boudjeltia, Intracranial aneurysms: wall motion analysis for prediction of rupture, American Journal of Neuroradiology 36 (10) (2015) 1796–1802, https://doi.org/10.3174/ajnr.A4357.
[69] L. Yang, X. Gao, C. Gao, S. Xu, S. Cao, Dynamic evaluation of unruptured intracranial aneurysms by 4D-CT angiography: comparison with digital subtraction angiography (DSA) and surgical findings, BMC. Med. ImAging 23 (1) (2023) 161, https://doi.org/10.1186/s12880-023-00983-x.
[70] S. Bolem, C. Valeti, N.T. Philip, B.J. Sudhir, B.S.V. Patnaik, Patient-specific arterial wall generation for intracranial aneurysms with a variable and a near realistic vessel wall thickness for FSI studies, Med. Eng. Phys. 130 (2024) 104211, https://doi.org/10.1016/j.medengphy.2023.104211.
[71] C. Valeti, S. Bolem, A.K. Alagan, B.J. Sudhir, S.K. Kannath, B. Akhade, et al., Influence of wall thickness on the rupture risk of a patient-specific cerebral aneurysm: a fluid–structure interaction study, Physics of Fluids 36 (9) (2024), https://doi.org/10.1063/5.0157736.
[72] A. Fedorov, et al., 3D Slicer as an Image Computing Platform for the Quantitative Imaging Network, Magn. Reson. Imaging 30 (2012) 1323–1341.
[73] S.G. Yazdi, P.H. Geoghegan, P.D. Docherty, M. Jermy, A. Khanafer, A review of arterial phantom fabrication methods for Flow measurement using PIV techniques, Ann. Biomed. Eng. 46 (11) (2018) 1697–1721, https://doi.org/10.1007/s10439-018-2085-8.
[74] ANSYS, ANSYS Fluent theory Guide, 2015. Canonsburg.

[75] H.K. Versteeg, W. Malalasekera, An Introduction to Computational Fluid Dynamics 2 (2007), https://doi.org/10.1002/9781119369189.
[76] F.C. Sales, A. Souza, F.R.S. Oliveira, R.A. Lima, J. Ribeiro, Stress Concentration on PDMS: an evaluation of three numerical constitutive models using digital image correlation, J. Mech. Behav. Biomed. Mater. 148 (Dec. 2023), https://doi.org/10.1016/j.jmbbm.2023.106164.
[77] A. Souza, G. Nobrega, L.B. Neves, F. Barbosa, J. Ribeiro, C. Ferrera, R.A. Lima, Recent Advances of PDMS In Vitro Biomodels for Flow Visualizations and Measurements: From Macro to Nanoscale Applications, Micromachines 15 (2024) 1317, https://doi.org/10.3390/mi15111317.
[78] I. Miranda, et al., Properties and Applications of PDMS for Biomedical Engineering : a Review, J. Funct. Biomater. 2 (1) (2022) 13, https://doi.org/10.3390/jfb13010002.
[79] C.A. Schneider, W.S. Rasband, K.W. Eliceiri, NIH Image to ImageJ: 25 years of image analysis, Nat. Methods 9 (7) (2012) 671–675, https://doi.org/10.1038/nmeth.2089.
[80] A.A. Valencia, A.M. Guzmán, E.A. Finol, C.H. Amon, Blood flow dynamics in saccular aneurysm models of the basilar artery, J. Biomech. Eng. 128 (4) (2006) 516–526, https://doi.org/10.1115/1.2205377.
[81] A. García-Galindo, R. Agujetas, J.R. López-Mínguez, C. Ferrera, Assessment of valve implantation in the descending aorta as an alternative for aortic regurgitation patients not treatable with conventional procedures, Biomech. Model. Mechanobiol. 22 (2) (2022) 575–591, https://doi.org/10.1007/s10237-022-01665-3.
[82] T. Wu, Q. Zhu, Advancement in the haemodynamic study of intracranial aneurysms by computational fluid dynamics, Brain Hemorrhages. 2 (2) (2021) 71–75, https://doi.org/10.1016/j.hest.2020.12.002.
[83] G.J. Riccardello, et al., Influence of relative residence time on side-wall aneurysm inception, Clin. Neurosurg. 83 (3) (2018) 574–581, https://doi.org/10.1093/neuros/nyx433.